CHAPTER 80

X-Ray Imaging of Phonon Interaction with Dislocations

DORON SHILO

and

EMIL ZOLOTOYABKO

Department of Materials Engineering, Technion-Israel Institute of Technology, Haifa 32000, Israel

Dislocations in Solids
Edited by F. R. N. Nabarro and J. P. Hirth

Contents

1. *Introduction*

Phonon-dislocation interaction has a strong effect on various materials properties. For example, phonon-induced dislocation vibrations significantly influence all characteristics related to the phonon flux, such as thermalsuch as and acoustic attenuation. Besides that, interaction of moving dislocations with phonons determines the viscosity coefficient in the dislocation motion, which in turn controls the dislocation dynamics.

The interaction between dislocations and phonons has been extensively studied for decades. Nevertheless, the established experimental methods (internal friction and thermal conductivity measurements) suffer from two principal disadvantages that hamper the studies in this field. First, the existing methods provide only averaged information over an ensemble of dislocations, with neither spatial nor temporal resolution. In other words, we are unable to resolve the interaction of phonons with individual dislocations, which is the subject of theoretical models. Secondly, the existing methods can be applied (and have been applied) only to ductile crystals, such as metals and alkali halides. Ductile crystals are characterized by high viscosity of dislocation motions, which results in the slowing down of dislocation movements. As shown later on, the viscosity coefficients in brittle ceramic crystals, such as $LiNbO_3$, may be 2–3 orders of magnitude lower than in ductile crystals.

In order to overcome these difficulties and limitations we have developed a new imaging technique, called high-frequency stroboscopic X-ray topography. It allows us to visualize, on the same image, the deformation fields of both individual acoustic wave fronts and vibrating dislocations. In order to visualize rapidly changing dynamic deformation fields, we conduct high-frequency stroboscopic measurements in which the acoustic wave propagation is synchronized with X-ray bursts coming from a synchrotron source to the sample position. Comprehensive theoretical analysis enabled us to find optimal experimental conditions for enhanced contrast. We also found a way to apply this technique to non-piezoelectric crystals. Due to these developments, it is now possible to visualize an interaction of short wavelength (down to 6 μm) surface acoustic waves with individual dislocations in a wide variety of crystals.

X-ray images, which were taken from $LiNbO_3$ crystals excited by surface acoustic waves, revealed significant distortions of acoustic wave fronts in the vicinity of dislocation lines. We showed that these distortions are related to the dynamic deformation field of the vibrating dislocation string. A theoretical model developed enabled us to simulate the overall dynamic displacement field, which is a combination of the displacement fields of the surface acoustic waves and the vibrating dislocations. By comparing the experimental and simulated images, the amplitudes and velocities of individual vibrating dislocations were determined for the first time.

It was found that dislocations can reach nearly "relativistic" velocities (close to the speed of shear bulk waves) under the subtle strains generated by acoustic waves. This is because

of the very low viscosity of dislocation motion in $LiNbO_3$, being at least 2 orders of magnitude lower than any value measured until now in all previously investigated materials.

Stroboscopic X-ray imaging in the GHz frequency range, as reviewed in this chapter, significantly expands the ability to investigate dislocation interactions with phonons in single crystals, including brittle ceramics, which were beyond the scope of the established experimental techniques.

The chapter is written to encompass all the information required to introduce the reader fully into the subject. Section 2 presents the relevant background of the theory of dislocations (with a focus on their dynamics) and comprises a survey of experimental methods and theoretical models for studying their interaction with phonons. In Section 3, the principles of stroboscopic X-ray imaging of acoustic waves are explained and the experimental technique is described in detail. Section 4 is devoted to the application of this method for studying the interaction of acoustic waves with individual dislocations in brittle ceramic crystals, such as $LiNbO_3$.

2. *Survey of dislocation interaction with phonons*

2.1. Dislocation dynamics

The motion of dislocations in their gliding plane is generally determined by the following equation [1]:

$$m^* \frac{\partial^2 \xi}{\partial t^2} - T \frac{\partial^2 \xi}{\partial l^2} + B \frac{\partial \xi}{\partial t} = F_{Ext} - F_P - F_{Bar}, \tag{1}$$

where ξ describes the temporally and spatially dependent deviation of the dislocation shape from a straight line situated along an energetically favored lattice direction.

The first term on the left side represents the dislocation inertia, where the effective mass per unit length is approximately $m^* \cong 0.5\rho b^2$, with ρ being the material density and $\boldsymbol{b}$ the Burgers vector. The second term on the left side gives the resistance of the dislocation to its elongation, where the line tension, $T \approx 0.5\mu b^2$, approximately equals the energy per unit length of the dislocation line [1–3], with μ being an effective shear modulus. The values of m^* and T depend on the dislocation character (e.g., edge, screw or mixed dislocation), and the ratio between them,

$$\sqrt{\frac{T}{m^*}} = \sqrt{\frac{\mu}{\rho}} = V_T \tag{2}$$

defines the shear wave velocity, V_T, which also gives the speed of the atomic movements along the dislocation line.

The third term on the left side of eq. (1) describes the viscous resistance to dislocation motion. The viscosity coefficient, B, is governed mainly by phonon interactions with the moving dislocation. The viscosity significantly affects not only the dislocation dynamics, but also the phonon propagation within the crystal. Thus, the dislocation interaction with

phonons plays a significant role in such phenomena as heat conductivity [4,5] and attenuation of acoustic waves [6,7].

The terms on the right hand side of eq. (1) describe forces per unit length that act on the dislocation line. The expression F_{Ext} is the force exerted by the external stress, σ_{ij}, on a unit of dislocation length, and it is given by the expression [8]

$$F_{Ext} = \sum n_i \sigma_{ij} b_j, \tag{3}$$

where the vector **n** with components n_i is a unit vector normal to the glide plane.

The term F_P on the right side of eq. (1) is called the Peierls force [9] and is caused by the periodic lattice potential applied to the dislocation line. The Peierls potential appears as a periodic array of valleys and hills in the glide plane. The Peierls force is typically expressed as [9]

$$F_P = \sigma_P b \sin\left(\frac{2\pi\xi}{a}\right) \tag{4}$$

where σ_P is the external stress required to overcome the Peierls potential barrier (i.e. to move the dislocation out of a potential valley), and a is the distance between adjacent potential valleys, which as a rule is equal to the shortest lattice translation. Note, that for screw and mixed dislocations the vectors a and b are not parallel and hence are not necessarily equal. Nevertheless, since b also tends to follow the shortest lattice translation, in many cases $a = b$. The ratio σ_P/μ_{eff} is roughly 10^{-4} in fcc metals, 10^{-3} in bcc metals and ionic crystals, and 10^{-2} in covalent crystals such as silicon [1].

The term, F_{Bar}, on the right side of eq. (1) represents local forces exerted on the dislocation line by defects, such as precipitates or other dislocations. These defects typically form pinning points which prevent the dislocation motion across a crystal.

By using eq. (1), one can predict both the steady-state shape of a dislocation line and the mode of dislocation motion. Let us consider, for example, a single crystal which during its growth or during annealing treatment is subjected to elevated temperature and no external forces (i.e. $F_{Ext} \cong 0$). In the steady state, the time derivatives of ξ are equal zero. If the density of pinning points is low, there exist rather long dislocation segments, for which $F_{Bar} \cong 0$. These segments obey the following stationary equation

$$T\frac{\partial^2\xi}{\partial l^2} - \sigma_P b \sin\left(\frac{2\pi\xi}{a}\right) = 0 \tag{5}$$

which follows from eq. (1) by setting all parameters mentioned above to zero and using eq. (4) for the Peierls force.

The trivial solution of eq. (5), $\xi = 0$, describes a dislocation line which is located within a single Peierls potential valley. This is extremely rare since the dislocation segments are, generally, pinned with their ends located at different potential valleys. In this case, there is competition between the first term of eq. (5), which acts to straighten the pinned dislocation line, and the second term, which tries to confine the dislocation segment within a certain potential valley. In a crystal, in which the second term is dominant, the dislocation lines

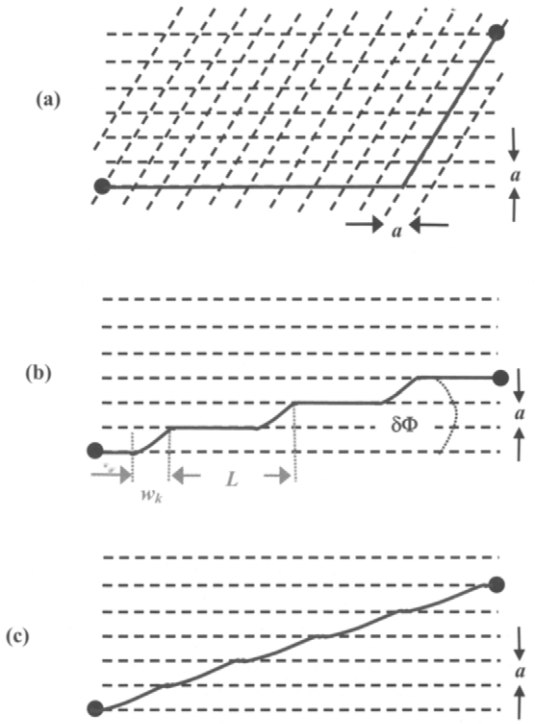

Fig. 1. Possible shapes of dislocation lines, which are pinned at two points located in different Peierls valleys (indicated by dashed lines): (a) – dislocation line is composed of long segments, which are completely confined to Peierls valleys; (b) – dislocation line is composed of short segments which are located in Peierls valleys and connected by kinks, which pass over potential barriers, (c) – nearly straight dislocation line, which is not confined to Peierls valleys.

are typically confined within Peierls valleys and form shapes as illustrated in Fig. 1(a). A classic example of such a crystal is silicon [10].

If the second term of eq. (5) is not dominant, the dislocation line can follow another solution of eq. (5) that describes a more complicated dislocation shape (see Fig. 1(b)). In this case, it is composed of segments located in adjacent Peierls valleys and connected by small fragments called "kinks" [2]. Thus, the dislocation line can link the two pinning points by forming a set of kinks as illustrated in Fig. 1(b). For geometrical kinks the average distance between two adjacent ones is

$$L = a/\delta\Phi \tag{6}$$

where $\delta\Phi$ is the angle between the direction of the Peierls valleys and a straight line that connects the pinning points. The width of an individual kink is given by [2]:

$$W_k = a\left|\left(\frac{\partial l}{\partial \xi}\right)_{\xi=a/2}\right| = a\sqrt{\frac{\pi T}{2ab\sigma_P}} \tag{7}$$

and is typically between a few and a few tens of lattice parameters.

The effect of the Peierls potential on dislocation motion depends on the ratio between L and W_k. If $L \gg W_k$, the majority of the dislocation line is confined to Peierls valleys (as illustrated in Fig. 1(b)), and the entire dislocation segment is subjected to the Peierls force which hampers its motion. In contrast, if $L \leqslant W_k$, the dislocation line is no longer confined to Peierls valleys (see Fig. 1(c)), and correspondingly, the dislocation motion is no longer subject to Peierls forces.

Considering the dislocation motion under the general eq. (1), one can indicate three different regimes corresponding to three specific intervals of the external force. If F_{Ext} is larger than both F_{Bar} and F_P, the dislocation movement in the long term will be governed by viscosity resistance. According to eq. (1), after a short time the dislocation will reach a uniform steady state velocity

$$BV_d = F_{Ext}, \tag{8}$$

where $V_d = \partial\xi/\partial t$.

If the external force is in the range, $F_P < F_{Ext} < F_{Bar}$, the dislocation line can be pinned as a whole, but segments located far from the pinning points can easily move. If the dislocation can get away the pinning points by thermal activation, its motion will be determined by the combined effect of the activation rate at the pinning points and the viscous motion between the pinning points.

In the range where F_{Ext} is smaller than both F_{Bar} and F_P, the dislocation segment can overcome the Peierls potential by a thermal activation process only. This is done by a formation of "bulges" on the dislocation line, which are composed of two kinks and a very short fragment between them (see stage (a) in Fig. 2). After the formation of a bulge, the kinks move in opposite directions along the Peierls valley and thus drag the dislocation line to the neighboring valley (see stages (b) and (c) in Fig. 2). The stress required to move kinks parallel to the potential valleys is very small; h ence, kinks typically move in viscous mode. The kinks that are formed by this mechanism are called "thermal kinks", in contrast to geometrical kinks which were depicted in Fig. 1(b).

It becomes clear from the above analysis that the viscous resistance to dislocation motion plays a significant role in dislocation dynamics. As follows from eq. (1), the viscosity coefficient, B, is the only parameter whose magnitude is not *a priori* known because of

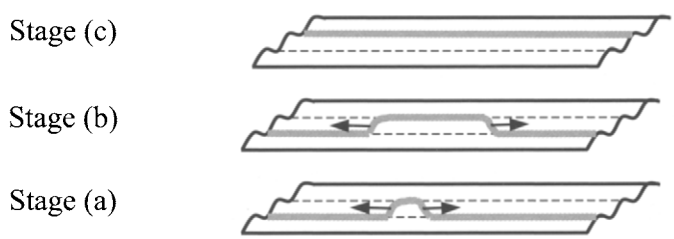

Fig. 2. Thermally activated motion of a linear dislocation over the Peierls barrier. Stage (a) – formation of a bulge, which consists of a pair of kinks and a short segment already situated in the adjacent Peierls valley. Stage (b) – movement of the kinks in opposite directions along the Peierls valley. Stage (c) – drag of the entire dislocation line into the adjacent Peierls valley.

the complexity of viscosity mechanisms. Therefore, there is a necessity for experimental studies aimed at obtaining viscosity coefficients to dislocation motion for different materials.

2.2. Viscous drag of dislocations

It is possible to divide the mechanisms of viscous drag of dislocations into three categories which are described below.

2.2.1. General viscous behavior

The dynamic deformation accompanying the dislocation motion can be considered in terms of elastic waves that create an excess of phonons and disturb the local phonon equilibrium. The dispersion and absorption of the non-equilibrium phonons results in a viscous resistance to dislocation motion. The viscous behavior is a general property of a crystal, which causes an attenuation or drag to any waves, not only to those that are generated by moving dislocations. For example, waves that create a local excess of phonons can be caused by temperature gradients or by an external excitation of acoustic waves. Therefore, the mechanisms that are responsible for general viscous behavior also affect the heat conductivity and attenuation of acoustic waves.

There are different mechanisms for the dispersion and absorption of phonons in crystals. The dominant is phonon-phonon interaction, the theory of which was developed by Akhiezer [11]. As was shown later on in Ref. [12], phonon–phonon interactions significantly contribute to the overall viscosity coefficient of dislocation motion. Similar to the phonon interaction with the "phonon gas", there also exists interaction with the "electron gas" [13], but its effect is much weaker, even in metals [1,14]. Another mechanism that causes the dispersion and absorption of excess phonons is due to the thermoelastic effect, which reveals itself in changing temperatures under stress. Hence, the dislocation motion is accompanied by heat transfer and thereby causes an energy loss.

2.2.2. "Phonon wind" – scattering of phonons due to non-linear elastic behavior

In this mechanism, phonons are scattered by the deformation field of the dislocation due to small changes in the material density and elastic modules (the detailed description of this effect is given in Section 2.4). Phonon scattering influences the attenuation of acoustic waves due to their scattering by static dislocations and the resistance to dislocation motion due to the scattering of the crystal phonons by moving dislocations. In the coordinate system of a moving dislocation, the phonons propagate with the same speed as the dislocation moves, but in the opposite direction. This "phonon wind" transfers momentum to the dislocation line opposite to the dislocation motion, with momentum proportional to the dislocation velocity. Calculations [15] showed that this mechanism usually makes an important contribution to the overall viscosity coefficient.

2.2.3. Acoustic emission

Time-dependent changes of the dislocation velocity and related kinetic energy losses are a source of acoustic emission [14]. Local velocity changes are due to interactions with

crystal defects or thermal fluctuations. The latter is called "fluttering" and has a similar effect on thermal conductivity and attenuation of acoustic waves. The Peierls potential also causes small perturbations of the dislocation velocity as the dislocation line moves from valleys to hills and so forth (the radiation friction effect). Calculations [14] showed that the mechanisms of acoustic emission are relatively weak, and their influence is only important under certain conditions such as low temperatures or very high Peierls barriers.

2.2.4. *Viscosity coefficients in different materials*

It can be concluded that the viscosity coefficient of dislocation motion is a result of phonon interactions with moving dislocations. Most of the described mechanisms for viscous drag of dislocations also have a significant effect on the heat conductivity and attenuation of acoustic waves.

The room temperature viscosity coefficients, B, of dislocation motion, measured by different methods described in the next section, are summarized in Table 1. The wide ranges of measured B-values (hundreds of percent) are, in part, due to the uncertainty of the dislocation character and partially due to large errors inherent to some of the experimental techniques. Due to limitations of conventional experimental methods, the variety of crystals in which the viscosity coefficients were measured is also very limited and restricted to metals and alkali-halides, which are ductile at room temperature. The typical viscosity coefficients in ductile materials are rather high, ranging from 0.1 to 3 mPoise.

In brittle materials, the viscosity coefficients are much smaller and cannot be measured by conventional methods. In order to evaluate them one can assume the proportionality between the viscosity coefficient, B, and *total* acoustic wave attenuation, α. This assumption is well justified for general viscous behavior (see Section 2.2.1) for which a mechanical viscosity, η, can be defined, and it can be proven that both $B \propto \eta$ [12,14] and $\alpha \propto \eta$ [7]. Other types of viscosity mechanisms, including the phonon wind and acoustic emission, also affect both the B- and α-values, but not necessarily in the same proportion.

The room-temperature values of the acoustic attenuation, α, for different types of materials are summarized in Table 2, which shows remarkable variation among groups containing metals, semiconductors, and insulating ceramics. The typical α-values for semiconductors are an order of magnitude smaller than those for metals, and the typical α-values for insulating ceramic crystals are 2–3 orders of magnitude smaller than in metals. This fact motivates the study of dislocation motion in insulating ceramic crystals such as the ones used in acoustic devices due to their low acoustic attenuation.

Table 1
Measured values of the viscosity coefficient, B, of dislocation motion in single crystals at room temperature (Ref. [14])

Crystal	LiF	NaCl	KCl	KBr	Cu	Al	Pb	Zn	Nb
B (mPoise)	0.3–1.3	0.1–0.3	0.3–0.8	1.7–2.0	0.1–0.9	0.2–3.1	0.4	0.4–2.5	0.2

Table 2
Total acoustic attenuation coefficients (at 1 GHz) in cubic single crystals at room temperature (Ref. [7])

Crystal	Propagation direction	Wave mode	Attenuation coefficient (dB/m)
Metals			
Al	⟨110⟩	Longitudinal	7500
Cu	⟨100⟩	Longitudinal	27000
Au	⟨110⟩	Longitudinal	20000
Semiconductors			
Si	⟨100⟩	Longitudinal	1000
	⟨111⟩	Longitudinal	650
Ge	⟨100⟩	Longitudinal	2300
	⟨100⟩	Shear	1000
Ceramic insulators			
MgO	⟨100⟩	Longitudinal	330
	⟨100⟩	Shear	40
Strontium titanate	⟨100⟩	Longitudinal	600
Yttrium iron	⟨100⟩	Longitudinal	200
garnet	⟨100⟩	Shear	34
Yttrium aluminum	⟨100⟩	Longitudinal	20–32
garnet	⟨100⟩	Shear	110

2.3. Experimental methods for studying phonon interaction with dislocations

Until our research, there were three conventional experimental methods for studying the phonon interactions with dislocations: measurement of dislocation mobility, internal friction, and measurement of heat conductivity.

2.3.1. Measurements of dislocation mobility

This method [14,16] is based on the measurement of the distance, Δx, that individual dislocation propagates under application of a stress pulse with an amplitude σ, and duration, Δt. If the stress value is high enough to provide $F_{Ext} \gg F_{Bar}$, F_P (see eq. (1)) the whole dislocation line, after a short time, τ_0, reaches the steady state velocity, $V_d(\sigma)$, as was explained in Section 2.1. Substituting $F_{Ext} = \sigma b$ (see eq. (3)) in eq. (8), yields:

$$BV_d = \sigma b. \tag{9}$$

The dislocation velocity is calculated as $V_d = \Delta x/\Delta t$, which is valid until $\tau_0 \ll \Delta t$, and after that the B-value is extracted using eq. (9). In order to measure the distance, Δx, selective etching of dislocation pits before and after the application of the stress pulse is done, followed by the subsequent measurement of the distance between pits by optical or electron microscopy. The accuracy to measure the B-value for an individual dislocation is about 30%.

At room temperature, this technique can be used only for ductile materials since brittle materials are subjected to fracture before the dislocation motion starts (i.e. at smaller

stresses). By using this technique, brittle materials can be investigated only at elevated temperatures (when strictly speaking they are no longer brittle). Unfortunately, the results of these studies cannot be extrapolated to room temperature because the mechanism of dislocation motion is changed with temperature (thermal activation instead of viscous drag (see Section 2.1)).

Except the overall value of B, this method does not provide any information concerning the details of phonon interaction with dislocations and its sensitivity to the phonon frequency and structure of the dislocation line. Dislocation vibrations under an excitation of acoustic waves, which play very important role in heat conductivity and attenuation of acoustic waves, are beyond the scope of this technique.

2.3.2. *Internal friction*

In this method [3], the effect of vibrating dislocations on acoustic wave propagation is probed by measuring the changes of the acoustic wave attenuation and velocity as functions of its frequency and amplitude. These measurements provide information, not only on the overall value of B but also on the specific mode of interaction between a dislocation and acoustic wave. The majority of experimental results were explained in the framework of the vibrating string model, developed by Granato and Lücke [3], which describes the vibration of pinned dislocation segments (for details see Section 2.5.2).

The B-value is determined by measuring the asymptotic limit of the acoustic wave attenuation, α_∞, at frequencies much higher than the resonance frequencies. According to the vibrating string model, the part of α_∞ which is caused by dislocation vibrations, is given by [17]:

$$\alpha_\infty^{\mathrm{dis}} = \frac{4\chi\mu b^2 N}{\pi^2 B V_T}, \tag{10}$$

where N is the density of free dislocation segments, and χ is the Schmid factor. The latter connects the acoustic stress tensor to the effective shear resolved stress that acts on the dislocation line in its glide plane. In order to extract the $\alpha_\infty^{\mathrm{dis}}$-values from measured α_∞-coefficients, the acoustic attenuation is taken twice, before and after gamma irradiation. Point defects, generated by the radiation, prevent the dislocation motion and hence $\alpha_\infty^{\mathrm{dis}}$ is nearly given by the difference between α_∞-values measured before and after sample irradiation.

Evaluation of the density of free dislocation segments in eq. (10) is more problematic since the dislocation lines most often have multiple pinning points and cannot vibrate. This complication is overcome by using specimens subjected to plastic deformation at room temperature with no annealing. In such specimens the majority of dislocations are free to move. The experimental procedure limits the implementation of internal friction technique to ductile materials only.

2.3.3. *Measurements of heat conductivity*

The principle of this method is similar to that one used for the internal friction measurements, but now the subject is an effect of vibrating dislocations on heat conductivity. The heat conductivity at low temperatures is determined by measuring the traveling time of a

thermal pulse excited by a laser [18]. An improved technique comprises two-dimensional mapping of the thermal pulse propagation [5,19] and allows one to study heat conductivity along different crystal directions.

In this method, as for the internal friction technique, one has to separate the net effect of dislocation vibrations from other interactions which influence the heat conductivity. This is accomplished by doing measurements before and after plastic deformation at room temperature, and hence this method is also limited by applications to ductile materials.

2.3.4. Drawbacks of conventional experimental methods

We repeat that the described experimental methods suffer from two principal disadvantages that hamper the studies in this field. The first is that the methods for studying the phonon interaction with dislocations (i.e. internal friction and heat conductivity measurements) provide only averaged information on the ensemble of dislocations with neither spatial nor temporal resolution. In other words, they are not able to probe the phonon interaction with individual dislocations, which is the subject of theoretical models (see Section 2.5). There is an attempt to overcome this problem (see Section 2.5.2) by summing the effect of numerous dislocations having different geometrical parameters. This approach is problematic since the strength of interaction changes by several orders of magnitude depending on geometrical factors, which may be very different for individual dislocations. Moreover, the result of the summation depends on some poorly defined parameters such as the average length of free dislocation segments, which can hardly be measured and may vary within several orders of magnitude.

Another disadvantage of the existing techniques relates to the fact that they can be applied (and have been applied) only in ductile crystals such as metals and alkali halides. Ductile crystals are characterized by high viscosity coefficients (see Section 2.2.4), which result in sluggish dislocation motion. As is mentioned in Section 2.2.4 and shown recently by us in Ref. [20], the viscosity coefficients in brittle ceramic crystals, such as $LiNbO_3$, may be 2–3 orders of magnitude lower than in ductile crystals. Correspondingly, the velocities of dislocation segments can reach very high values (close to the speed of sound) which cannot be measured experimentally.

In order to overcome these difficulties we developed a fast time-resolved X-ray visualization technique which simultaneously gives the images of the propagating acoustic wave and of the vibrating dislocation (see Section 3). In order to analyze these images, the theoretical models dealing with phonon scattering by dislocations should be revised. This is done in Sections 2.4–2.5.

2.4. Theoretical models describing the scattering of acoustic waves by the dislocation strain field

This section deals with scattering of acoustic waves by a static dislocation or by a dislocation which moves with no relation to acoustic waves. In this case, the acoustic waves are scattered due to non-linear elastic behavior in the vicinity of the dislocation line. In other words, the scattering mechanism is based on the changes of the acoustic wave speed

caused by strain-induced modification of material density and elastic modules. The overall effect of the strain field on the acoustic wave speed can be expressed, as [21]:

$$\frac{V_i - V_i^0}{V_i^0} = -\sum_{jk} \gamma_{jk}^i \varepsilon_{jk}, \tag{11}$$

where V_i and V_i^0 are the acoustic wave speeds with and without the strain field, respectively, ε_{jk} is the strain tensor, and γ_{jk}^i is the tensor of Gruneisen constants which are of the order of 1. The index i denotes a specific mode of acoustic waves. For example, putting the strain field of screw dislocation in an isotropic material [1], $\varepsilon = b/4\pi r$ (with r being the distance from the dislocation line), into eq. (11), yields

$$\frac{\Delta V_i}{V_i^0} = -\frac{\gamma^i b}{4\pi r}. \tag{12}$$

The changes in the acoustic velocity cause refraction of the acoustic wave when it crosses the dislocation line. In order to evaluate the refraction effect, one can use geometrical optics, giving the scattering angle of the order of $\Delta V_i / V_i$. This approach is justified at distances r larger than the acoustic wavelength, λ. Therefore, for $r > \lambda = 5$ μm, $b = 0.5$ nm, and $\gamma^i = 1$, the scattering angle is of the order of 10^{-5} rad or smaller.

Comprehensive calculations, based on the quantum scattering theory [22–24], also proved that the acoustic wave refraction by static dislocations has negligible effect on the acoustic wave propagation as compared with the effect of the dynamic interaction of acoustic waves and dislocations, which is considered in the next section.

2.5. Theoretical models for the dynamic interaction of acoustic waves with dislocations

Dynamic interaction between an acoustic wave and dislocation means that a whole dislocation line or some of its segments are vibrating under the applied acoustic stress field. In general, the dislocation vibrations cause rather strong changes in the attenuation and velocity of the acoustic waves. More specifically, they lead to the wave field distortions of the primary acoustic wave and the emission of secondary acoustic waves. There are different modes of dislocation vibrations which require appropriate modeling. In the subsequent sub-sections, we will distinguish between three types of dislocation vibrations which relate to three different types of dislocation dynamics as mentioned in Section 2.1.

First, we will analyze the situation when F_{Ext} (i.e. the force applied to the dislocation by the acoustic stress field) is larger than both F_{Bar} and F_P, and a whole dislocation line moves uniformly. The second type of motion arises when $F_P < F_{Ext} < F_{Bar}$ and corresponds to dislocation segments pinned at both their ends, which vibrate as strings. In the third case, the dislocation line is confined within Peierls potential valleys (i.e. $F_{Ext} < F_P$) and only very limited dislocation motion is permitted.

2.5.1. Vibrating dislocation in a uniform motion

Eshelby and Nabarro [25,26] developed a model that describes uniform motion of a free dislocation, which is not subjected to pinning barriers, Peierls barriers, or viscous resistance. The solution is given for a screw dislocation under the influence of a bulk shear wave. The model calculations focus on the displacement field, Δu_z^{dis}, of the vibrating screw dislocation, which is located parallel to the z-axis and vibrates in the x-direction according to

$$\xi = \xi_0 \cos(\omega t + \phi), \tag{13}$$

where $\omega = 2\pi f$ is the circular vibration frequency and ϕ is the phase shift of the dislocation vibration with regard to the acoustic wave.

At distances, $r \ll \lambda$, the displacement field follows the local shape modification of the dislocation line, and hence, it can be expressed as a displacement field of static dislocation, $\mathbf{u}^{\text{dis}}$, located at $x = \xi(t)$. Thus, the dislocation vibration forms a dynamic displacement field, which near the dislocation line is given by:

$$\mathbf{\Delta u}^{\text{dis}} = \mathbf{u}^{\text{dis}}(x - \xi, y) - \mathbf{u}^{\text{dis}}(x, y). \tag{14}$$

Eq. (14) is valid for any dislocation which vibrates in any mode of motion. In the model described the expression for specific displacement field of screw dislocation in an isotropic material [1,27]:

$$u_z = \frac{b}{2\pi} \tan^{-1}\left(\frac{y}{x}\right) \tag{15}$$

was substituted to eq. (13).

Note that the combination of displacement fields described by eqs (14) and (15) does not satisfy the wave equation, and, hence, it cannot be used to obtain the dynamic displacement field in a whole medium. Moreover, the time which is needed for elastic deformation to arrive at the regions far away from the dislocation line is much larger than the time period of the dislocation vibrations and hence eq. (14) is not valid in the range, $r \gg \lambda$. Eshelby and Nabarro [25,26] looked for a solution which satisfies both a general wave equation at $r \gg \lambda$ and eqs (14)–(15) at $r \ll \lambda$. They suggested the following expression for the dynamic displacement field (in cylindrical coordinates (r, φ)):

$$\Delta u_z^{\text{dis}} = A_0 u_0 \sin\varphi \left[J_1(kr) \cos(\omega t + \phi) + Y_1(kr) \sin(\omega t + \phi) \right], \tag{16}$$

$$A_0 = -\frac{\pi}{\ln(4/kb) - \gamma - 1/2}, \tag{17}$$

where k is the acoustic wave vector, J and Y are the Bessel functions of the first and second kinds, respectively, and $\gamma = 0.5772$ is the Euler constant. The displacement amplitude, u_0, relates to the strain amplitude of the acoustic wave by $\varepsilon_{yz}^0 = 1/2ku_0$. A comparison

of the asymptotic behavior of this solution with eqs (14) and (15) provides the vibrating amplitude:

$$\xi_0 = \frac{2A_0\varepsilon^0_{yz}\lambda^2}{\pi^2 b}. \tag{18}$$

Recently, Maurel et al. [28] developed more general approach which allows obtaining solutions for any dislocation character. They applied it to both screw and edge dislocations and showed important distinctions that arise when considering different dislocation character and various polarizations of the acoustic waves.

2.5.2. The vibrating string model

This model describes the vibrating dislocation segment, having a length L_0 and pinned at both its ends. The appropriate equation of motion is

$$m^*\frac{\partial^2\xi}{\partial t^2} - T\frac{\partial^2\xi}{\partial z^2} + B\frac{\partial\xi}{\partial t} = \sigma b, \tag{19}$$

which is derived from eq. (1) by neglecting F_P and using F_{Bar} to describe the pinning properly. The acoustic stress field, σ, is given by

$$\sigma = \sigma_0 \exp\left(-\alpha^{\mathrm{dis}}x\right)\cos(\omega t - x/V) \tag{20}$$

where V is the acoustic wave velocity, which is influenced by the vibrating dislocations and hence is a function of ω. The model assumes that partial attenuation coefficient, α^{dis}, due to vibrating dislocations depends on frequency, ω.

The solution of eqs (19) and (20) is given by the series [3]

$$\xi = \frac{4\sigma b}{m^*}\sum_{n=0}^{\infty}\frac{1}{2n+1}\sin\left[\frac{(2n+1)\pi z}{L}\right]H_n(\omega,\omega_n)\cos(\omega t - \phi_n), \tag{21}$$

$$H_n(\omega,\omega_n) = \left[\left(\omega_n^2 - \omega^2\right)^2 + \left(\omega\Omega\right)^2\right]^{-1/2}, \tag{22}$$

$$\Omega = \frac{B}{m^*}, \tag{23}$$

$$\omega_n = (2n+1)\frac{\pi}{L_0}V_T = \frac{2n+1}{2}\frac{\lambda}{L_0}\omega \tag{24}$$

and

$$\tan\phi_n = \frac{\omega\Omega}{\omega_n^2 - \omega^2}. \tag{25}$$

Extraction of the expression $\omega_n^2 - \omega^2$ from eq. (25), its substitution to eq. (22), and utilizing some trigonometric transformations yields the simplified expression for H_n:

$$H_n = \frac{|\sin\phi_n|}{\omega\Omega}. \tag{26}$$

In a majority of situations, the first term ($n = 0$) in the expansion series (eq. (21)) dominates [3]. In any case it is possible to learn something about the behavior of the system by considering the first term only. In this approximation, using the relationship, $\sigma_0 = \mu\varepsilon_0$, as well as eqs (23) and (26), the dislocation vibrations can be written as

$$\xi = \xi_0 \sin\left(\frac{\pi z}{L_0}\right)\cos(\omega t - \phi_0), \tag{27}$$

with amplitude

$$\xi_0 = \frac{4\mu\varepsilon_0 b}{B\omega}|\sin\phi_0|. \tag{28}$$

Further summation over the dislocation ensemble allows obtaining expressions for the acoustic parameters which are measured by internal friction, i.e. the attenuation coefficient and the acoustic wave velocity. Keeping only the first term in the series (21), these parameters can be expressed as:

$$\alpha^{\text{dis}} = \frac{\xi_0}{\lambda}\frac{2\chi bN}{\pi\varepsilon_0}|\sin\phi| = \frac{4\chi\mu b^2 N}{\pi^2 B V_T}\sin^2\phi_0 \tag{29}$$

and

$$\frac{V - V_T}{V_T} = -\frac{\chi' V_T^2 N}{\omega\Omega}|\sin 2\phi_0|, \tag{30}$$

where N is the density of dislocation segments that can glide freely and χ' is some geometrical factor smaller than 1.

Substituting the values of B, typical to metals and alkali-halides from Table 1 into eq. (23), yields $\Omega \approx 200$ GHz. Hence, in all the internal friction experiments $\omega \ll \Omega$. Moreover, according to eqs (25)–(26), at frequencies much larger than resonant frequencies (i.e. $\omega \gg \omega_n$), the value of $|\sin\phi_0|$ is approximately 1. Therefore, eq. (29) transforms to eq. (10), which was used for evaluation of the B-values in Section 2.3.

The vibrating string model is appropriate if one can neglect the Peierls force. However, usually the Peierls barrier, σ_P, is larger than the acoustic stress amplitude. Yet the vibrating string model is valid for dislocation lines that are initially not confined to the Peierls potential valleys, as illustrated in Fig. 1(c). It turned out that this situation is very common, at least in fcc metals. If a majority of the dislocation lines is initially located within the Peierls valleys, other models described in the next section should be used.

2.5.3. Vibrating dislocations located within the Peierls potential valleys

Dislocations that are confined to Peierls valleys may exhibit limited vibrating motion in three forms:

(1) Dislocation segments which are located at the bottom of potential valleys vibrate within these valleys. Modeling of this problem can be found in Refs [25,29].
(2) The acoustic waves produce bulges on the dislocation line similarly to the case of thermally activated kinks (see Fig. 2). In this case, there exists a resonance frequency which depends on the activation energy for bulge formation and is temperature dependent [1,2].
(3) Kinks which initially exist will vibrate along a direction parallel to Peierls valleys. Such kinks will also interact with other neighboring kinks, this interaction being non-linear. It is possible to obtain a set of linear equations by approximating the kink motion by small amplitude vibrations [2,29]. If the kink density is high enough to allow a collective motion of the dislocation line, the results of this model [2] are similar to those obtained by the vibrating string model.

2.5.4. Concluding remarks

The dynamic interaction of acoustic waves with dislocation results in three main effects: (i) attenuation of acoustic waves; (ii) motion of vibrating dislocations, and (iii) emission of secondary acoustic waves. The strength of interaction regarding all the effects mentioned is determined by a single parameter ξ_0/λ, i.e. the ratio of the vibrating amplitude, ξ_0, and the acoustic wavelength, λ. According to eq. (29), partial attenuation of the acoustic wave due to dislocation vibrations is proportional to ξ_0/λ. The overall speed of dislocation motion is determined by the amplitude of its velocity, $V_{d0} = \xi_0\omega$, which is also proportional to ξ_0/λ. The strain field amplitude of the emitted acoustic waves at far distances from the dislocation line is determined by $\Delta u_0^{\text{dis}} k_f$, where Δu_0^{dis} is the amplitude of the displacement field $\Delta \mathbf{u}^{\text{dis}}$ and k_f is the wave vector of the emitted waves. As a rule, Δu_0^{dis} is proportional to the amplitude of the dislocation motion, ξ_0, and k_f is approximately equals to $2\pi/\lambda$. Hence, the strain field amplitude of the emitted acoustic waves is approximately proportional to ξ_0/λ. Thus, in each effect, the strength of the dynamic interaction is determined by $\xi_0/\lambda \propto \xi_0\omega$.

According to eq. (28) the product, $\xi_0\omega$, is proportional to $1/B$. Hence, the insulating ceramic crystals, which are expected to have very small viscosity coefficients of dislocation motion (see discussion in Section 2.2.4), should also reveal a very strong dynamic interaction between acoustic waves and dislocations.

The existing models of dynamic interaction of acoustic waves with dislocations describe only a small part of the possible interaction modes. In particular, it turned out that the specific solution of the equation of motion for individual dislocations is strongly influenced by many geometrical parameters, such as the dislocation character, its orientation with respect to an acoustic wave, the length of the free dislocation segments, etc. Since the conventional experimental methods do not allow resolving the interaction of acoustic waves with individual dislocations and do not provide information about these geometrical parameters, there is an inherent difficulty in formulating a model which can be used to interpret the experimental results in this field (see examples in Refs [4,5]).

3. Stroboscopic X-ray imaging of acoustic waves

The survey in Section 2 emphasizes the necessity for the development of experimental methods that are sensitive to an interaction of acoustic waves with individual dislocations and provide comprehensive information on the dislocation character and acoustic wave parameters. These requirements are met in the stroboscopic X-ray diffraction imaging (stroboscopic X-ray topography) which, in principle, allows us to visualize the deformation fields of acoustic wave fronts and vibrating dislocations in the same image. Visualization of acoustic wave fronts provides complete information on acoustic wave propagation and scattering processes since the normals to the wave fronts indicate the local direction of energy flow. Note that the acoustic wave fronts can be visualized by other methods, e.g., optically [30], acoustically [31] or by scanning electron microscopy [32]. However, only stroboscopic X-ray diffraction imaging has a unique capability to simultaneously "look" at both the traveling acoustic waves and lattice defects, such as dislocations and, hence, to probe the interaction between them.

In order to achieve time-resolved visualization of acoustic waves, one has to first of all avoid time averaging of the dynamic deformation field induced by propagating acoustic waves in the crystal. For this purpose, the investigated samples are illuminated by X-ray pulses that are much shorter than the period of acoustic vibrations (see Fig. 3). However, since the number of X-ray quanta in a single pulse is not enough for the formation of the X-ray image (actually we need about 10^9 pulses per image even working with modern synchrotron sources), we use the stroboscopic principle of registration, which allows a data accumulation for long periods of time without destroying the phase relations between the acoustic wave and X-ray burst periodicities.

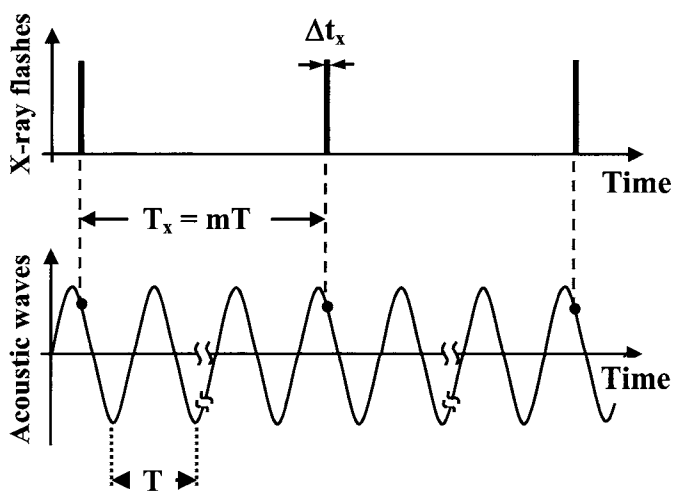

Fig. 3. The principle of stroboscopic measurement. In a given crystal point, all incident X-ray bursts interact with periodic deformation fields having exactly the same magnitude and phase.

This is achieved by phase locking the acoustic signal to the X-ray burst periodicity created by the electron bunch pattern within the synchrotron storage ring. As a necessary condition, the acoustic frequency, $f = mf_x$, should be an integer multiple of the X-ray burst frequency, f_x. Being synchronized with an acoustic wave, every X-ray burst probes the same instantaneous deformation field during the entire exposure [33]. As a result, the rapidly oscillating deformation field of the acoustic wave, propagating at the speed 3–5 km/s, is revealed in the diffraction images as if frozen in time.

The experimental setup, which we use for stroboscopic X-ray topography at the ID19 beam line of the European Synchrotron Radiation Facility (ESRF, Grenoble, France), is schematically illustrated in Fig. 4. It is based on the capability of modern synchrotron X-ray sources to provide very short bursts (of about 50 ps) of high intensity coherent X-rays, which are strictly periodic in time. The electronic signal from the synchrotron storage ring, having exactly the same frequency, $f_x = 5.68$ MHz, as the X-ray bursts, is applied to a frequency synthesizer which produces the output phase-locked signal of a multiple frequency, $f = mf_x$. The value of m is chosen to provide the output frequency, f, to be as close as possible to the resonance frequency of the interdigital transducer (IDT) deposited on top of the sample. The high-frequency output signal is then amplified and applied to the interdigital transducer, which generates surface acoustic waves (SAW). The stroboscopic X-ray diffraction image from the vibrating crystal is collected by using special X-ray photographic film with a spatial resolution down to 0.5 μm.

SAW are particularly suitable for the X-ray imaging in the Bragg scattering geometry since the acoustic energy is concentrated within a thin layer (with a thickness of the order of the SAW wavelength) beneath the sample surface, which is comparable to the X-ray penetration depth. Furthermore, SAW can be excited to have shorter wavelengths by an order of magnitude than those characteristic for bulk acoustic waves. Short wavelengths

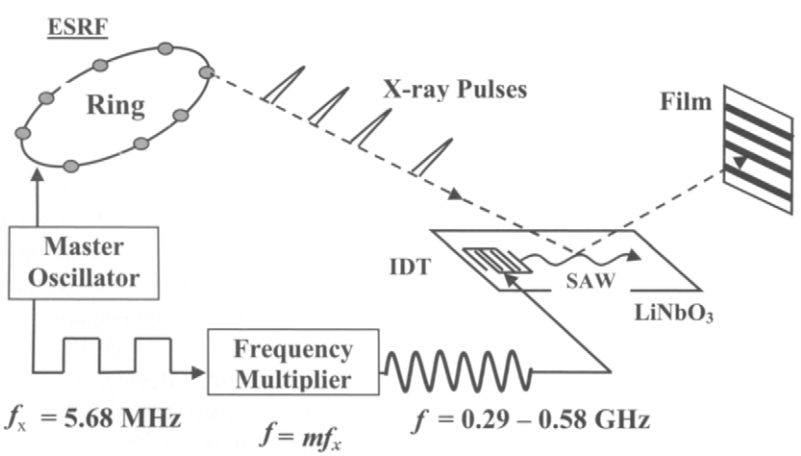

Fig. 4. Schematic illustration of the experimental setup for the stroboscopic X-ray imaging experiments. The sinusoidal signal inserted to the interdigital transducer (IDT) is phase locked with the X-ray bursts.

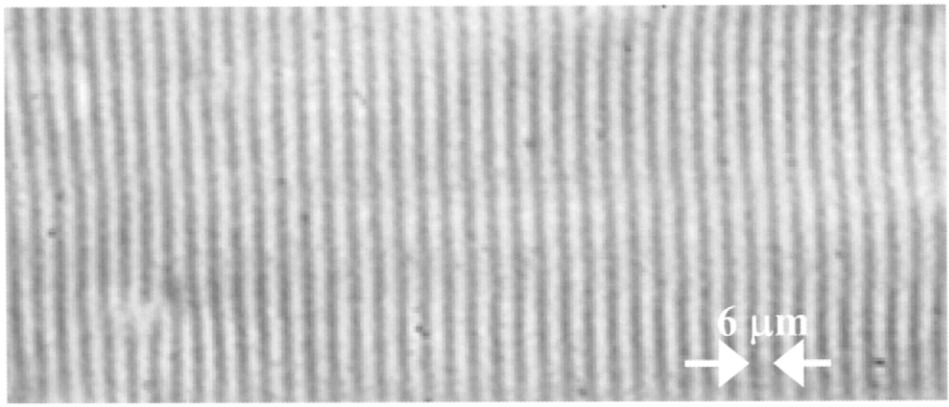

Fig. 5. Stroboscopic X-ray diffraction image of a 0.58 GHz SAW propagating in $LiNbO_3$ with the speed of 3.5 km/s. The spacing between individual acoustic wave fronts equals 6 μm.

are especially important for visualizing the acoustic wave interaction with crystal defects of low dimensionality, such as dislocations.

The first stroboscopic synchrotron X-ray diffraction experiments aimed at visualizing traveling acoustic waves in crystals were performed in the early 1980s with a 30 MHz SAW [34,35]. Because of the relatively large SAW wavelength (about 100 μm) those experiments did not exhibit phonon interactions with dislocations. An attempt at the stroboscopic X-ray imaging with a 500 MHz SAW was reported in Ref. [36], but those days it was impossible to resolve short individual acoustic wave fronts because of the limited coherence of the X-rays used. A breakthrough in this field has been achieved in experiments that we performed with 0.29 GHz (i.e. 12 μm) SAW devices at ESRF [33,37]. The images obtained exhibited well-resolved individual acoustic wave fronts and their local distortions in the vicinity of dislocation lines. However, because of the non-optimized image contrast in these initial experiments, it was hard to quantitatively investigate the interaction of acoustic waves with dislocations.

Detailed analysis of the X-ray focusing and de-focusing process by SAW [38] allowed us to find optimal experimental conditions for enhanced contrast in the stroboscopic X-ray diffraction images. As a result, we succeeded to visualize individual acoustic wave fronts of a 6 μm SAW ($f = 0.58$ GHz) with excellent contrast allowing quantitative image analysis [39]. An example of such an image is shown in Fig. 5, in which alternating dark and bright lines are individual acoustic wave fronts of the high-frequency SAW propagating through a crystal. This image provides a 'snapshot' of the dynamic deformation field which actually changes with a periodicity of 1.6 ns.

The experiments mentioned above were performed with SAW devices, which were fabricated on top of specifically oriented highly piezoelectric crystals ($LiNbO_3$) (see Fig. 6). A development of a modified technique allowed us to apply the stroboscopic X-ray imaging to weakly- and non-piezoelectric crystals [40]. This has been achieved by transferring SAW from an external piezoelectric transducer to the crystal investigated by generating evanescent acoustic waves via viscous liquid as a coupling medium. The modified tech-

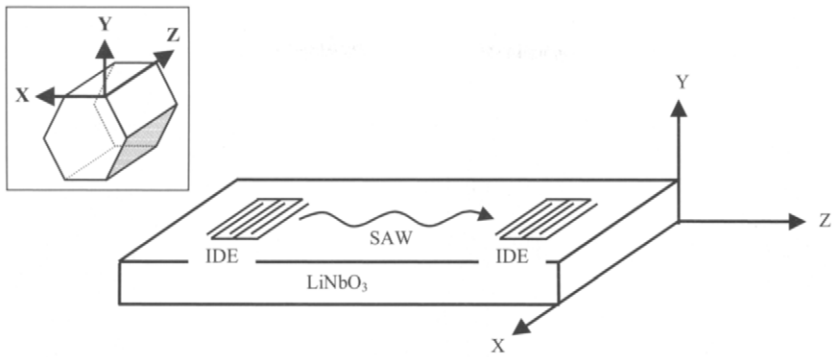

Fig. 6. SAW device, comprising an interdigital transducer (IDT) on top of $LiNbO_3$ crystal. Insert shows Cartesian coordinate system (X,Y,Z) related to hexagonal unit cell of $LiNbO_3$.

nique provided images of a 0.29 GHz SAW propagating in Si and GaAs as is demonstrated in Fig. 7.

These technical developments were crucial for the establishment of the stroboscopic X-ray diffraction imaging as a regular method to study acoustic wave (phonon) interaction with dislocations, which is the subject of the next section.

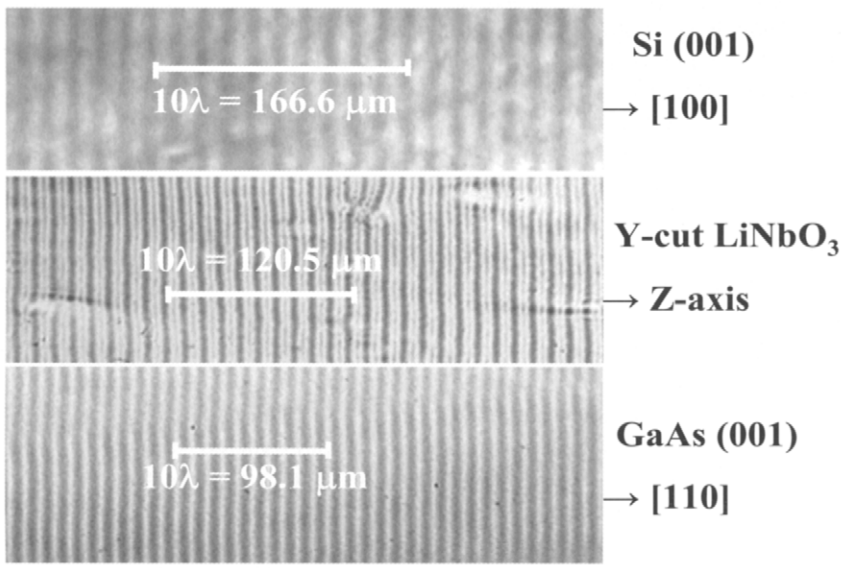

Fig. 7. Stroboscopic X-ray diffraction images of a 0.29 GHz SAW in Si (upper panel), GaAs (lower panel) and $LiNbO_3$ (in the middle). Material-dependent changes in the SAW wavelength, reflecting the differences in the SAW velocity, are clearly seen.

4. *Interaction of acoustic waves with individual dislocations in brittle ceramics*

The experimental results presented in this section, which helped us to understand the phonon interaction with dislocations in brittle ceramics, were obtained with $LiNbO_3$-based SAW devices. They were produced on the polished surfaces of the Y-cut $LiNbO_3$ wafers, 76 mm in diameter and 0.5 mm thick. For device fabrication, a system of sectioned interdigital electrodes, consisting of 1.5 μm wide metal fingers separated by the same width blank intervals, was deposited on top of the wafers by using standard lift-off photolithography. The doubled distance between adjacent electrodes, i.e. the SAW wavelength was 6 μm, which corresponded the SAW frequency, $f = 0.58$ GHz, for Z-propagating SAW. The second type of SAW devices utilized the electrode structure providing the SAW wavelength of 9.8 μm ($f = 0.355$ GHz). Stroboscopic diffraction images were taken from $LiNbO_3$ single crystals ((030) reflection) at X-ray energy of 10 keV, utilizing the 16-bunch mode of the ESRF storage ring operation ($f_x = 5.68$ MHz). The frequency multiplication coefficient was $m = 102$ for $f = 0.58$ GHz and $m = 63$ for $f = 0.355$ GHz.

4.1. Experimental results

A typical stroboscopic X-ray image revealing the propagation of a 6 μm SAW and its interaction with individual dislocations is shown in Fig. 8(a). Well-resolved acoustic wave fronts form alternating dark and bright lines that pass like a ruler through the entire image area. Besides that, the traces of five dislocation segments are also visible. Dislocations (dark lines) are better resolved in the image shown in Fig. 8(b), which was taken for comparison from exactly the same crystal area, but after switching off the SAW. The two long dislocation segments are almost parallel to the surface since their visible lengths are in the range of tens of microns, whereas the X-ray penetration depth under experimental conditions was only 9 μm.

In the vicinity of the dislocation lines, strong wave front deflections occur (see Fig. 8(a)). In particular, in the vicinity of the two long dislocation segments, wave front deflections are clearly visible as black streaks forming large angles with acoustic wave fronts *existing* far away from the interaction region. We show later on that these deflections arise as a result of the dislocation movements under SAW excitation. Similar features of the deflected wave fronts were found in all images taken from different samples and using SAW excitation of different wavelengths. For example, distortions in a 9.8 μm SAW wave front, when crossing the dislocation line, are clearly seen in Fig. 9.

Such strong wave front deflection in a range of several microns around the dislocation line cannot be explained in terms of the acoustic wave scattering by the static strain field of individual dislocation. Following the discussion in Section 2.4, the effect of the static dislocation strain field on the refraction angle at a distance of several microns from the dislocation line should be of the order of 10^{-5} rad, which is 3–4 orders of magnitude lower than that observed in Figs 8 and 9. Thus, we can unambiguously conclude that the wave front deflections visualized are related to vibrating dislocations (see Section 2.5) which are involved into dynamic interaction with acoustic waves (phonons).

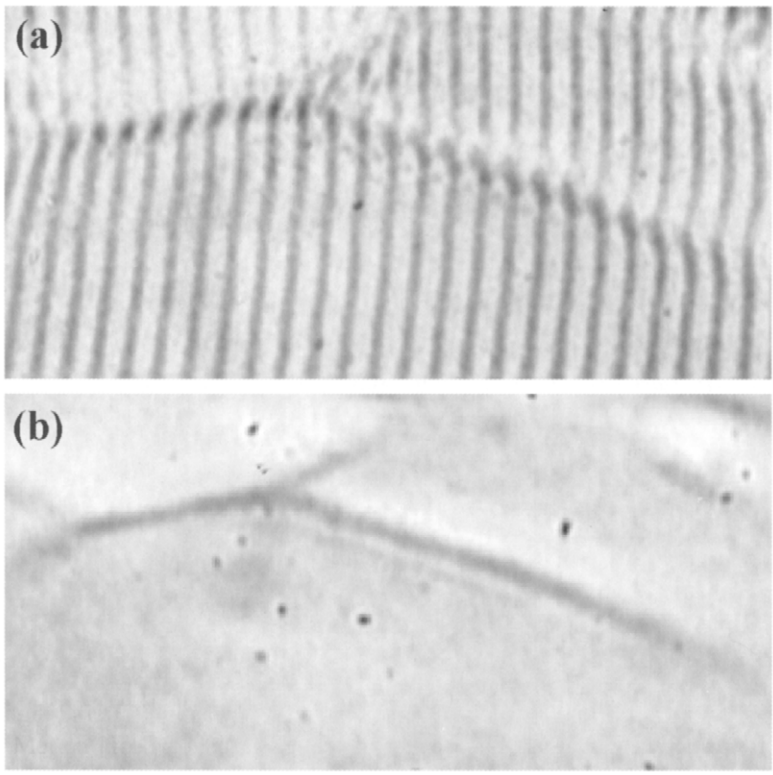

Fig. 8. (a) Stroboscopic X-ray diffraction image of a 0.58 GHz SAW propagating in $LiNbO_3$ and its interaction with linear dislocations. Remarkable wave front deflections in close vicinity to dislocation lines are clearly seen. The spacing between non-distorted individual acoustic wave fronts equals 6 μm. (b) Stroboscopic X-ray diffraction image taken from exactly the same crystal region as in (a), but with no SAW excitation. Images are taken from Ref. [20].

Additional support of this idea comes from the following observation: deflection of acoustic wave fronts is a common feature for all dislocation lines situated along the crystal surface, except those that are parallel to the Z-axis of $LiNbO_3$. An example of such behavior is shown in Fig. 10, which reveals pronounced wave front deflections in the left part of the dislocation line only. Wave-front deflections are practically absent in the right part of the dislocation line that is nearly parallel to the z-axis (the acoustic wave fronts far away from the dislocation line are perpendicular to the z-axis). As is explained in Section 4.3, dislocation lines parallel to the z-axis are confined to Peierls potential valleys and can hardly participate in high amplitude vibrations.

4.2. Theoretical model and simulations

In order to explain experimental data and extract quantitative information on dislocation vibrations and related parameters, a model for simulating the observed X-ray images was

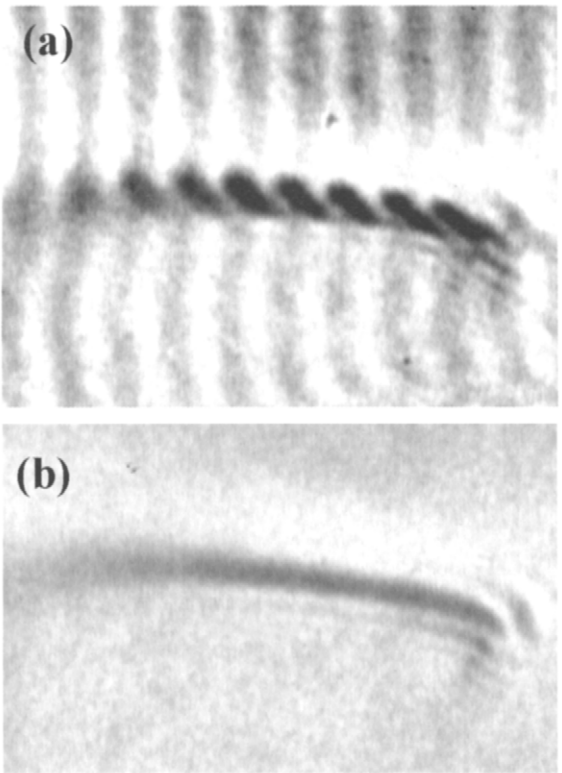

Fig. 9. (a) Stroboscopic X-ray diffraction image of a 0.355 GHz SAW propagation in $LiNbO_3$ revealing pronounced wave front distortions in close vicinity to dislocation line. The spacing between non-distorted individual acoustic wave fronts equals 9.8 μm. (b) Stroboscopic X-ray diffraction image taken from exactly the same crystal region as in (a), but with no SAW excitation.

developed *by us* [20], which is based on the calculation of the dynamic deformation field of a vibrating dislocation. Most of the known models in this field (see Section 2.5), deal with calculating the effect of dislocation vibrations far away from the dislocation line. This approach is not suitable for our purpose since experimentally the wave front deflections are observed in a limited space (less than the one acoustic wavelength, λ) around the dislocation line. Keeping this in mind, we adopted the approach of Eshelby and Nabarro [25,26] (see also Section 2.5.1) for calculating the displacement field of the vibrating dislocations close to the dislocation line. A combination of the dynamic displacement fields of the SAW and of the vibrating dislocation was then used for simulating the local shapes of acoustic wave fronts and comparing them with the observed features in the X-ray images. Note that the X-ray contrast is not always proportional to the amplitude of atomic displacement, so the exact dependence can be more complicated [38]. Nevertheless, the local geometrical shapes of alternating dark and bright lines in X-ray images follow the local shapes of acoustic wave fronts which are determined by the combined displacement field.

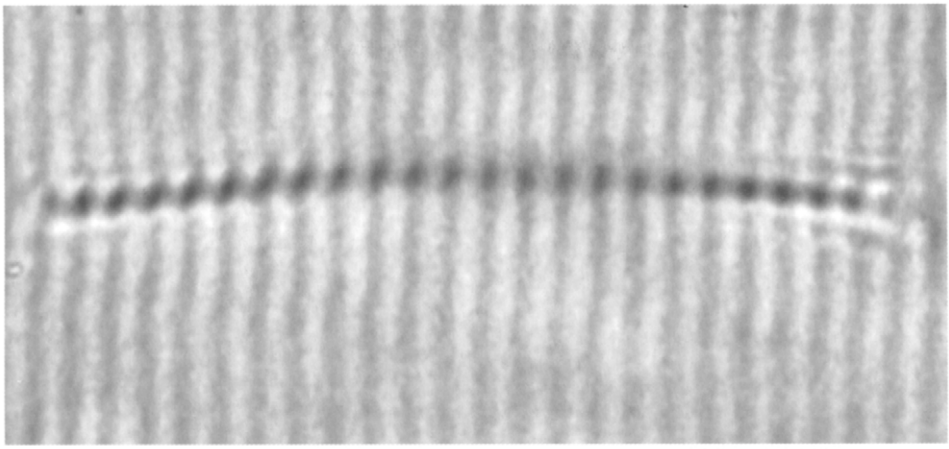

Fig. 10. Stroboscopic X-ray diffraction image showing an interaction of a 0.58 GHz SAW with a dislocation line which is almost parallel to the crystal surface. On the left side of the dislocation segment, remarkable deflections of acoustic wave fronts are clearly visible. On the right part of the dislocation segment, which is parallel to the Z-crystallographic direction of $LiNbO_3$, the SAW wave fronts remain undistorted. The spacing between non-distorted individual acoustic wave fronts equals 6 μm.

In order to describe the displacement field of the SAW, $\mathbf{u}^S$, we used an orthogonal coordinate system (x, y, z) (see Fig. 11), with the y-axis normal to the crystal surface and the z-axis parallel to the SAW wave vector, $\mathbf{k}_s$. The Bragg scattering geometry is sensitive only to the u_y component of the displacement vector, $\mathbf{u}$. In the case of SAW [41]:

$$u_y^S = u_{y0}(y)\cos(k_s z - \omega t). \tag{31}$$

An auxiliary coordinate system (x', y', z') is related to the vibrating dislocation, with the z' axis parallel to the dislocation line (see Fig. 11). The X-ray topographs indicate that the dislocation lines, which strongly interact with the SAW, are almost parallel to

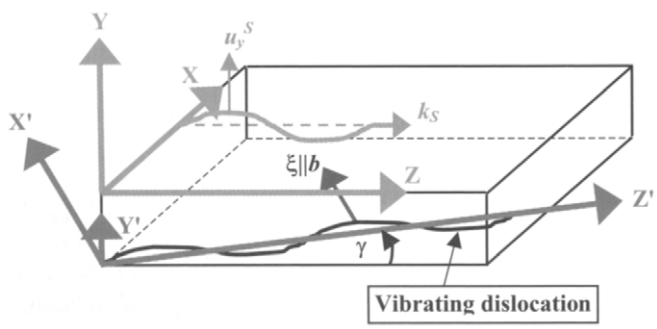

Fig. 11. The coordinate systems related to the propagating SAW (x, y, z) and the vibrating dislocation line (x', y', z').

the crystal surface. Hence, we chose the y' axis parallel to the y axis and the x' axis to be perpendicular to both the y' and z' axes, so that the x'–z' and x–z planes coincide. Since screw dislocations parallel to the crystal surface result in $u_y = 0$, the deformation fields were simulated for edge dislocations with Burgers vector, **b**, along the x' axis, i.e. perpendicular to the dislocation line (the z' axis). Practically, we have mixed dislocations, but the difference in the displacement component, u_y, between mixed and edge dislocation results in a geometrical factor close to one.

According to Eshelby and Nabarro (see Section 2.5.1), at distances $r \ll \lambda$ (counted outwards from the dislocation line) the displacement field of the dislocation follows the instantaneous location of the dislocation segments. If so, in order to find the displacement field of a vibrating dislocation we can use the known one for a static dislocation, u_y^{dis}, but taken in the locations, $x' = \xi(z', t)$, modified by the dislocation vibrations, ξ. Thus, the dislocation vibration creates a dynamic displacement field which, when close enough to the dislocation line, can be expressed as:

$$\Delta u_y^{\text{dis}} = u_y^{\text{dis}}(x' - \xi, y') - u_y^{\text{dis}}(x', y'). \tag{32}$$

As the static displacement field, u_y^{dis} in eq. (32), we used a well-known solution for an edge dislocation in isotropic medium [27]:

$$u_y^{\text{dis}}(x', y') = -\frac{b}{8\pi(1-\upsilon)}\left[(1-2\upsilon)\ln\left(x'^2 + y'^2\right) + \frac{x'^2 - y'^2}{x'^2 + y'^2}\right], \tag{33}$$

where υ is Poisson's ratio.

As is explained in Section 4.4, the solution of the dislocation's equation of motion, at time intervals much larger than the vibration period, is given by

$$\xi = \xi_0 \sin(k_d z' - \omega t + \phi), \tag{34}$$

where ξ_0 is the vibrating amplitude (real) and ϕ is the phase shift of dislocation vibration with respect to the phase of the SAW. The wave vector, k_d, is defined by the spatial periodicity of the force applied to dislocation by the SAW and is

$$k_d = k_S \cos\Phi, \tag{35}$$

where Φ is the angle between the dislocation line and k_s (i.e. between the z' and z axes). The ratio ξ_0/λ manifests the strength of the dynamic interaction between acoustic waves and dislocations (see Section 2.5.4) and determines the amplitude of the dislocation velocity

$$V_{d0} = \omega\xi_0 = 2\pi\frac{\xi_0}{\lambda}V_R, \tag{36}$$

where $V_R = \omega/k_S$ is the speed of the SAW.

Substituting eqs (33) and (34) into eq. (32), yields the expression

$$\Delta u_y^{\mathrm{dis}}(x', y') = -\frac{b}{8\pi(1-\upsilon)}\left[(1-2\upsilon)\ln\left[\frac{(x'-\xi_0\sin(k_d z'-\omega t+\phi))^2+y'^2}{x'^2+y'^2}\right]\right.$$
$$\left.+\frac{(x'-\xi_0\sin(k_d z'-\omega t+\phi))^2-y'^2}{(x'-\xi_0\sin(k_d z'-\omega t+\phi))^2+y'^2}-\frac{x'^2-y'^2}{x'^2+y'^2}\right]. \tag{37}$$

The total dynamic displacement field was calculated in the (x', y', z') coordinate system by adding expressions (31) and (37):

$$u_y = u_y^S + \Delta u_y^{\mathrm{dis}} \tag{38}$$

after the following coordinate transformation

$$x = x'\cos\Phi - z'\sin\Phi, \qquad z = x'\sin\Phi + z'\cos\Phi, \tag{39}$$

applied to eq. (31).

The time dependence of the displacement field is formally revealed in both eqs (31) and (37) containing the terms that depend on the product, ωt. However, in the stroboscopic mode of measurement, the X-ray pulses probe the displacement field at certain instants corresponding to $\omega t = 2\pi m$ (where m is an integer) and, hence, all periodic time dependences practically disappear.

Additional simplification comes when one considers depth dependent effects in the displacement fields. In this context, both eqs (31) and (37) depend on the coordinates y' and y. However, the influence of the y' and y values is revealed only in some changes of the amplitudes of u_y^S and $\Delta u_y^{\mathrm{dis}}$. Detailed simulations show that within a reasonable range of y' and y-values, which are smaller than the X-ray penetration depth (and also $y' < \lambda$), the exact choice of the y' and y-values does not significantly influence the overall displacement field map in the x'–z' plane.

As mentioned above, eq. (37) is valid for $r \ll \lambda$. Beyond this range, the solution is very complicated and can be derived only in specific simple cases [25,26]. We used eq. (37) in the range $|x'| < \lambda/2$ and neglected the dynamic displacement field of the dislocation line in the range, $|x'| > \lambda/2$. This neglecting is justified by two findings: (i) the displacement field (37) decays as ξ_0/r with the distance, r, from the dislocation line; (ii) experimentally, the wave front distortions were observed only in the range, $|x'| < \lambda/2$.

As an example of a simulation of the local shapes of acoustic wave fronts, the dynamic displacement map calculated for $\xi_0/\lambda = 0.14$ and $\phi = \pi/2$ is shown in Fig. 12 together with one of the experimental X-ray images. It can be seen that the simulated map reproduces all main features of the wave front distortions that appear in the X-ray image collected. The thin white lines, which were imposed artificially in order to follow the wave front distortions, are practically identical in both images. For a deeper understanding, we show two separate contributions to the dynamic deformation field in Fig. 13. In the middle of the map, the dynamic part of the dislocation deformation field, $\Delta u_y^{\mathrm{dis}}$, is presented for $|x'| < \lambda/2$. The right and left sides of the map show the SAW's contribution, u_y^S, in

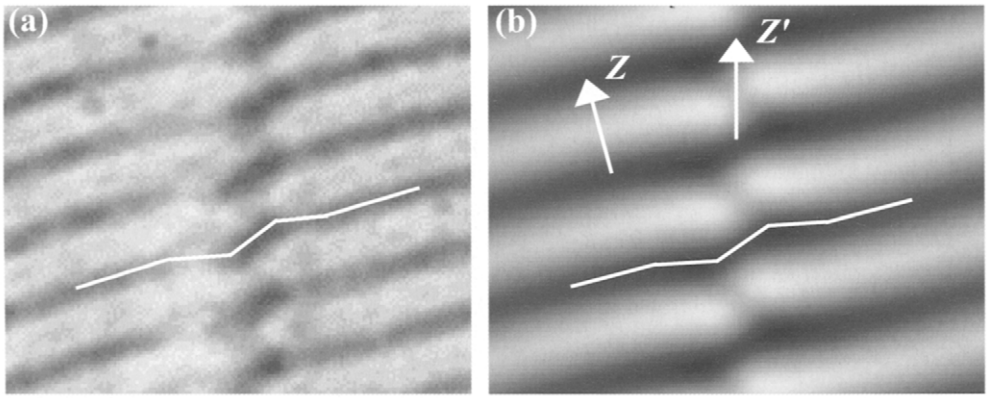

Fig. 12. Stroboscopic X-ray diffraction image (a), showing wave front deflections in the vicinity of a vibrating dislocation in $LiNbO_3$, as compared with the simulated map (b) of the total dynamic displacement field for $\xi_0/\lambda = 0.14$ and $\phi = \pi/2$. The spacing between non-distorted individual acoustic wave fronts equals 6 μm.

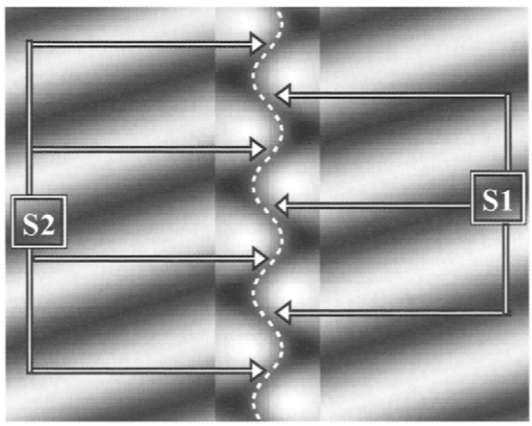

Fig. 13. Displacement fields of SAWs and the vibrating dislocation, shown separately, under the same conditions as in Fig. 12. The contribution of Δu_y^{dis} is drawn within $|x'| < \lambda/2$, while that of u_y^S – at $|x'| > \lambda/2$. The displacement field of the vibrating dislocation forms a zigzag pattern near $x' = 0$. Two types of segments that comprise the zig-zag pattern are indicated by S1 and S2. The instantaneous shape, $\xi(z')$, of the vibrating dislocation is shown by the broken white line.

the range of $|x'| > \lambda/2$. It can be seen that the term, Δu_y^{dis}, produces a dark "zigzag" like pattern, which is actually an image of the vibrating dislocation line, $\xi(z')$. The latter is calculated by the means of eq. (34) and indicated by a wavy vertical white line in Fig. 13. The angle between the zigzag segments and the z' axis becomes smaller as the normalized amplitude, ξ_0/λ, decreases.

In the total dynamic deformation field (see Fig. 12), some of the dark segments (indicated by S1 in Fig. 13) that form the zigzag pattern disappear since they are located exactly in the middle of the bright SAW wave fronts. Thus, the observed pattern in the vicinity of

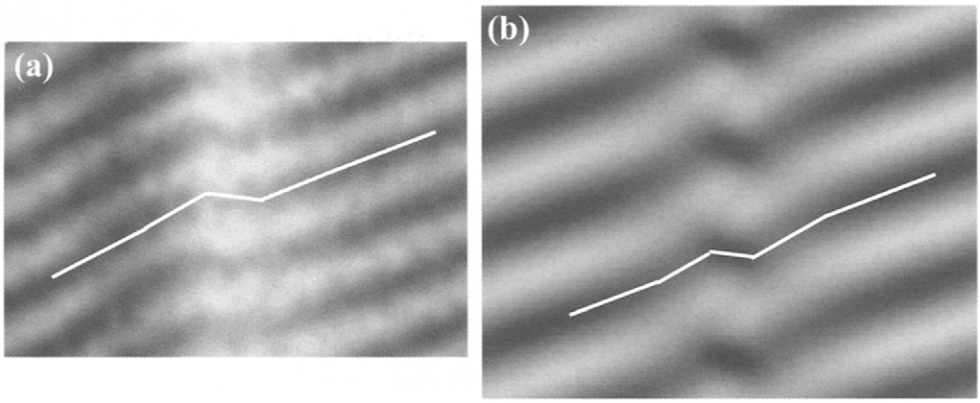

Fig. 14. Stroboscopic X-ray diffraction image (a) showing wave front distortions in the vicinity of a vibrating dislocation in $LiNbO_3$, as compared with the simulated map (b) of total dynamic displacement field for $\xi_0/\lambda = 0.14$ and $\phi = -\pi/2$. The spacing between non-distorted individual acoustic wave fronts equals 6 μm.

the dislocation line is actually an image of the second type of zigzag segments (indicated by S2 in Fig. 13), which remain in the image.

On the other hand, for $\phi = -\pi/2$, the S2 segments of the zigzag pattern disappear, and only the S1 segments remain in the image. As a result, the simulated map (see Fig. 14) exhibits dark streaks in the vicinity of the dislocation line, which are tilted by certain angles, as compared with Fig. 12. An example of the observed X-ray image of this type is also shown in Fig. 14.

Comparing the simulated maps with experimental images allowed us to extract the values of ϕ and ξ_0/λ for each individual vibrating dislocation that appeared in the collected X-ray images. It was found that the normalized amplitude (strength of phonon-dislocation interaction) is in the range of $\xi_0/\lambda = 0.08$–0.14 under a 6 μm SAW excitation and $\xi_0/\lambda = 0.02$–0.06 under a 9.8 μm SAW excitation. The lower vibration amplitude under an excitation of a 9.8 μm SAW is probably a result of weaker amplitude of SAW generated at a frequency which is shifted a few MHz away from the exact resonance value for a 0.355 GHz SAW transducer. For all vibrating dislocations the ϕ-values extracted from the displacement maps were found to be either $\phi = \pi/2$ or $\phi = -\pi/2$. As is explained in Section 4.4, this means that they vibrate in the resonant mode.

The amplitude of the dislocation velocity can be evaluated by substituting the extracted ξ_0/λ values into eq. (36), which yields $V_{d0}/V_R = 0.5$–0.88 for samples excited by a 0.58 GHz SAW. Using the relationship $V_T = 1.08V_R$, between the Rayleigh velocity, V_R, and shear bulk velocity, V_T, which is appropriate for YZ-$LiNbO_3$ [41], we obtain $V_{d0}/V_T = 0.46$–0.81. The dislocation velocities are 2–3 orders of magnitude higher than those previously measured in metals and alkali halides [3]. This result indicates that the dynamic interaction between acoustic waves and dislocations (see discussion in Section 2.5.4) in $LiNbO_3$ is several orders of magnitude stronger than that of metals and alkali halides. Moreover, a part of dislocations have the velocities not far from the velocity of shear bulk waves, V_T, which is considered to be the highest possible value of dislocation motion [1,27]. Until now such high dislocation velocities were observed only under extremely

high stresses [42]. The physical reasons for high dislocation velocities under subtle strains introduced by SAW will be clarified in the next section.

4.3. Dislocation analysis

As mentioned above, dislocations can move fast only if they are not subjected to Peierls barriers. In our case, the magnitude of the SAW-induced stress field (typically, $\sigma/\mu_{eff} < 10^{-4}$) is much smaller than the Peierls stress (typically, $\sigma_P/\mu_{eff} \approx 10^{-3}$–$10^{-2}$ for brittle ceramic crystals) and hence, the applied external force, F_{Ext}, is definitely smaller than the Peierls force, F_P (see eqs (3) and (4) as well as discussion in Section 2.1). Thus, the collected stroboscopic X-ray images give strong hints that the vibrating dislocations are not confined to Peierls potential valleys. This important point is demonstrated below by direct dislocation analysis in X-ray images.

According to Section 2.1, a dislocation does not "feel" the Peierls potential barrier if $L \leqslant W_k$, where L is the average distance between adjacent kinks and W_k is the width of an individual kink. Substituting eqs (6) and (7) into this inequality, yields:

$$\delta\Phi \geqslant \sqrt{\frac{2ab\sigma_P}{\pi T}}, \tag{40}$$

where $\delta\Phi$ is the angle between the direction of the Peierls valley and the whole dislocation line (see Fig. 1(c)). By using typical magnitudes of the parameters involved in eq. (40): $T \approx 0.5\mu_{eff}b^2$ [1–3], $a \cong b$, and $\sigma_P/\mu_{eff} \approx 10^{-2}$ [1], one obtains

$$\delta\Phi \geqslant 6.5°. \tag{41}$$

Important information about the directions of vibrating dislocations can be extracted from the collected X-ray images by measuring the angles, Φ_f, that dislocation images form with the z_f-axis, which is perpendicular to visible acoustic wave fronts (see Fig. 15). Performing this analysis, one has to keep in mind that the image of the dislocation line is a projection of its direction in a three-dimensional crystal onto the plane of the X-ray photographic film. For the X-ray scattering geometry that we used in our experiments (see Fig. 15), the following relations exist between the real crystal coordinate system (x, y, z) and the coordinate system (x_f, z_f) in the plane of the film:

$$\begin{aligned} x_f &= x\sin\theta - y\cos\theta, \\ z_f &= z, \end{aligned} \tag{42}$$

where θ is the Bragg angle for the X-ray reflection used. By using eq. (42), the angle Φ_f can be expressed as:

$$\Phi_f = \arctan\left(\left|\frac{l_x\sin\theta - l_y\cos\theta}{l_z}\right|\right), \tag{43}$$

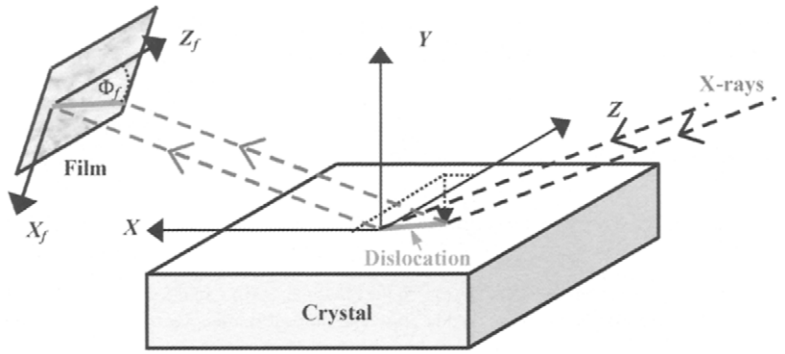

Fig. 15. Projection of a dislocation line on the X-ray photographic film.

where the vector $[l_x, l_y, l_z]$ denotes the direction of the dislocation line in the crystal. Using eq. (43), it is possible to understand whether or not the vibrating dislocation lines are confined to the Peierls potential valleys by calculating the difference between the magnitudes of Φ_f and Φ_f^P, the latter being related to the directions of the Peierls potential valleys in $LiNbO_3$.

For the reader's convenience, the glide systems for dislocations in $LiNbO_3$ and their possible Φ_f^P-values are summarized in Table 3. The left column specifies the three gliding systems known for $LiNbO_3$ [43]. The most common is the basal plane system (see Fig. 16(a)) with Burgers vectors, $|\mathbf{b}| = 0.5148$ nm, equal to **a** – translations of the hexagonal unit cell [44,45]. Supplementary gliding systems are the pyramidal and prismatic plane systems (see Figs 16 (b) and (c)). In both of them the smallest Burgers vectors, $|\mathbf{b}| = 0.5494$ nm, are along the directions $\frac{1}{3}\langle\bar{1}101\rangle$. The study [41] of the high temperature plastic deformation at $1070\,^{\circ}\mathrm{C} > 0.8T_m$ (T_m stands for melting temperature) showed that the critical resolved

Table 3
Directions of Peierls valleys for major glide systems in $LiNbO_3$. Angles, Φ_f^P, calculated by means of eq. (42), are placed in last column

Glide system	Possible directions of Peierls potential valleys	Cartesian axes $[l_x, l_y, l_z]$	Calculated $\lvert\Phi_f^P\rvert$
Basal	$\frac{1}{3}\langle 11\bar{2}0\rangle$	$[a, 0, 0]$	90°
$\frac{1}{3}\langle 11\bar{2}0\rangle\{0001\}$		$[a/2, a\sqrt{3}/2, 0]$	90°
		$[-a/2, a\sqrt{3}/2, 0]$	90°
Pyramidal	$\frac{1}{3}\langle\bar{1}101\rangle$	$[3a/2, a\sqrt{3}/2, c]$	3.46°
$\frac{1}{3}\langle\bar{1}101\rangle\{\bar{1}012\}$		$[-3a/2, a\sqrt{3}/2, c]$	27.67°
		$[0, a\sqrt{3}, c]$	30.33°
Prismatic	$\frac{1}{3}\langle\bar{1}101\rangle$	$[3a/2, a\sqrt{3}/2, c]$	3.46°
$\frac{1}{3}\langle\bar{1}101\rangle\{1\bar{2}10\}$		$[-3a/2, a\sqrt{3}/2, c]$	27.67°
		$[0, a\sqrt{3}, c]$	30.33°
	[0001]	$[0, 0, c]$	0

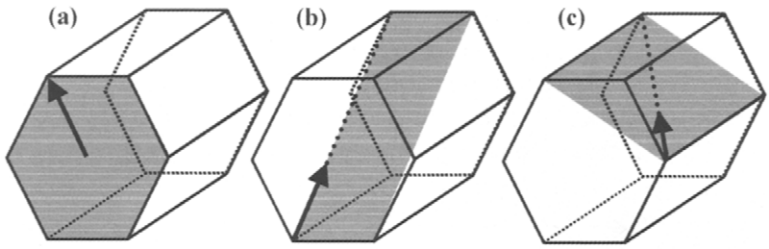

Fig. 16. Three major glide systems in $LiNbO_3$, (a) – in the basal plane, (b) – in the pyramidal plane, and (c) – in the prismatic plane. The glide planes are marked in gray. The shortest Burgers vectors are indicated by arrows.

shear stresses for these gliding systems are very similar. Taking into account also the proximity of Burgers vectors, it is reasonable to assume that dislocations related to all the three gliding systems can be formed during the crystal growth. As a rule, the directions of Peierls potential valleys and Burgers vectors form a two dimensional primitive unit cell within the gliding plane [1]. This consideration allowed us to indicate possible directions of Peierls potential valleys and calculate the Φ_f^P-values (the last column of Table 3) for each of the three gliding systems.

When analyzing the collected X-ray images, we found out that the values of Φ_f, measured for a large number of vibrating dislocations, do not fit the calculated ones. Instead, the measured angles are distributed in the range of $\Phi_f = 6°–20°$ with no bias toward any values. Furthermore, for most imaged dislocations, the difference between Φ_f and the nearest Φ_f^P-value was larger than 10°, and hence, it is reasonable to assume that the condition (41) is fulfilled.

This result strongly supports the conclusion that the vibrating dislocations are not confined to Peierls potential valleys that is a necessary condition for high speed dislocation movement. However, in a majority of metals and alkali halides, which are frequently investigated by the internal friction technique, the dislocations also are not confined to Peierls potential valleys [3], yet the measured dislocation velocities are much lower. In fact, to obtain such high dislocation velocities as we measured, the viscosity coefficient, B, for dislocation motion should be very small. The appropriate B value for $LiNbO_3$ can be extracted by analyzing the dislocation's equation of motion.

4.4. Extraction of the physical characteristics of vibrating dislocations

The equation of motion for dislocations not subjected to the Peierls force [1,2] can be written as:

$$m^* \frac{\partial^2 \xi}{\partial t^2} - T \frac{\partial^2 \xi}{\partial z'^2} + B \frac{\partial \xi}{\partial t} = F_{Ext}. \tag{44}$$

This equation is very similar to eq. (19), which was used by Lücke and Granato (see Ref [3] and Section 2.5.2). The only difference between their solution and the solution given below stems from the differences in the boundary conditions and a different application of the

external force, F_{Ext}, with regards to the dislocation line. The SAW-induced applied external force can be expressed by means of eq. (3) and Hooke's law, $\sigma_{ij} = c_{ijkl}\varepsilon_{kl}$, where ε_{kl} is the SAW's strain field, which is calculated by taking spatial derivatives $\partial u_i^S/\partial x_j$, of the SAW's displacement field, u_i^S (see, e.g., eq. (31)) and c_{ijkl} is the tensor of elastic moduli. The applied external force depends on the dislocation character and, generally can be written as:

$$F_{Ext} = \mu\varepsilon_0^{eff} b \sin(k_d z' - \omega t), \tag{45}$$

where ε_0^{eff} is an effective value of the SAW-induced strain amplitude, which actually depends on the dislocation character. In order to derive eq. (45), the equality $k_s z = k_d z'$, i.e. $k_s = k_d \cos\Phi$ (see eq. (35)), is used. Substituting eqs (2) and (44) into eq. (43) and dividing by $m^* \cong 0.5\rho b^2$ (see discussion in Section 2.1) yields the following normalized equation:

$$\frac{\partial^2\xi}{\partial t^2} - V_T^2\frac{\partial^2\xi}{\partial z'^2} + \Omega\frac{\partial\xi}{\partial t} = 2\frac{V_T^2}{b}\varepsilon_0^{eff}\sin(k_d z' - \omega t), \tag{46}$$

in which $\Omega = B/m^*$ according to eq. (23).

The solution of eq. (16) depends on the boundary conditions, which in our case can be imposed by using the geometrical parameters of individual vibrating dislocations deduced from the X-ray images. The capability to obtain this information is a significant advantage of the stroboscopic X-ray diffraction techniques over other non-diffraction methods. According to X-ray images (see, e.g., Figs 8 and 9), the vibrating dislocations are almost parallel to the crystal surface but yet have rather long parts propagating in depth. Therefore, the dislocation lines usually end at the surface, and this end is most probably not pinned. Concerning the second end, the X-ray images show that dislocations penetrate much deeper than the X-ray penetration length. Since the latter approximately equals to the SAW's penetration depth, we can conclude that a part of dislocation line excited by the SAW is free of pinning points. In that situation the dislocation vibrations will attenuate before they arrive at the dislocation end located in the crystal bulk and hence one can neglect the reflected wave from this end, even if it is pinned. Based on these considerations, it is reasonable to choose boundary conditions that correspond to a long dislocation string (much longer than the SAW wavelength), which is free at both its ends.

The solution of eq. (46) under the above mentioned boundary conditions and at times much larger than the vibration period is given by eq. (34). Substituting this solution into eq. (45), yields

$$\xi_0 = \frac{2V_T^2\varepsilon_0^{eff}}{b\Omega\omega}|\sin\phi| = \frac{\mu\varepsilon_0^{eff} b}{B\omega}|\sin\phi|, \tag{47}$$

where

$$\tan\phi = \frac{\Omega\omega}{V_T^2 k_d^2 - \omega^2}. \tag{48}$$

Eq. (48) is equivalent to eq. (25) that appears in the solution of Lücke and Granato [3], if one uses the relationship $\omega_0^2 = V_T^2 k_d^2$, where ω_0 is the dislocation's resonant frequency, which is not equal to ω. Substituting the relationship, $\omega = V_R k_s$, and eq. (35) into eq. (48), yields:

$$\tan\phi = \frac{\Omega}{\omega} \frac{1}{[(V_T/V_R)^2 \cos^2 \Phi - 1]}. \tag{49}$$

Based on eq. (49), it is easy to understand why the phase shift of the dislocation vibrations, extracted by comparing the experimental images and calculated dynamic deformation maps, was always close to $|\phi| \cong \pi/2$. In fact, setting $V_T/V_R \cong 1.08$ [41] and $0.94 < \cos\Phi < 1$ (for $\Phi < 20°$ as measured in the collected images), one finds that the denominator in eq. (49) is close to zero (resonance conditions), i.e. $|\phi| \cong \pi/2$. Moreover, since the exact value of V_T/V_R depends on the direction of the dislocation line, the denominator in eq. (49) can be either slightly positive or negative, providing the phase shift with both signs, $\phi \cong \pi/2$ or $\phi \cong -\pi/2$. As shown in Section 4.2, a change of the sign of ϕ from $-\pi/2$ to $+\pi/2$ causes sign changing in wave front deflections when crossing the dislocation line (compare Figs 12 and 14). An image of two dislocation lines located in the same crystal region and producing wave front deflections of both negative and positive signs is given in Fig. 8(a).

The viscosity coefficients, B, for dislocation motion in $LiNbO_3$ were evaluated by substituting the obtained values of $|\phi| \cong \pi/2$ and $\xi_0/\lambda = 0.08$–0.14 as well as the experimental and material parameters: $\mu = 60$ GPa, $\varepsilon_0^{eff} = 5 \times 10^{-5}$, $b = 0.55$ nm, and $\omega = 2\pi \times 0.58$ GHz, into eq. (47). Such evaluated B-values are in the range of $B = (5$–$9) \times 10^{-6}$ Poise, i.e. 2–3 orders of magnitude lower than those measured in metals and alkali halides [14]. The obtained results correlate well with the very low total acoustic attenuations, α, in $LiNbO_3$ and other brittle ceramic crystals (see discussion in Section 2.2) as compared with ductile materials.

A last remark relates to possible effect of SAW on other types of dislocations in $LiNbO_3$. Note that the right-hand term in eq. (47) is similar to the solution by Lücke and Granato [3], which appears in eq. (28). A comparison between these two equations allowed us to conclude that the vibration amplitude in model [3] is even four times higher than in our model. This fact has an important implication on the subject, since dislocations in the basal gliding system of $LiNbO_3$ have the geometry that was considered in model [3] (i.e. a dislocation line is perpendicular to the acoustic wave propagation). Thus, these dislocations can indeed vibrate with very large amplitudes as follows from the well established model [3]. Unfortunately, we are not able to visualize these specific dislocation vibrations since in the scattering geometry used, the traces of these dislocation lines in the X-ray images are parallel to the acoustic wave fronts. Nevertheless, the phonon-induced vibrations of these dislocations may have a significant effect on the attenuation of acoustic waves in $LiNbO_3$.

4.5. Conclusions

In this chapter we showed that stroboscopic X-ray diffraction imaging provides unique information on the phonon-induced motions of individual dislocations. The key point of the

technique developed is the phase locking of the periodic high-frequency deformation field (affecting the dislocation movement) to the periodic X-ray illumination. In such a way, fast dislocation dynamics (on a ns to sub-ns scale) can be investigated as if it is frozen in time. It should be emphasized that the X-ray diffraction imaging technique is the only method allowing to "see" in one image the static and dynamic deformation fields with spatial resolution better than 0.5 μm and thus to study the dynamic interaction of dislocations with acoustic waves (phonons). Due to high spatial and temporal resolution, this technique is able to probe an elementary phonon interaction with an individual dislocation, which is a subject of theoretical analysis.

By using this technique we succeeded to visualize individual acoustic wave fronts in a GHz range. Due to improved imaging contrast we were also able to resolve the wave front distortions when crossing the dislocation lines. We showed that the observed wave front deflections are caused by dislocation vibrations, as a result of the interaction with phonons. For quantitative image analysis, we developed a model which allowed us to simulate the dynamic displacement maps containing both contributions of SAW and vibrating dislocations. By comparing experimental images and simulated dynamic displacement maps, the amplitude and velocity of vibrating dislocations were extracted. Further solution of the dislocation's equation of motion, using boundary conditions that were deduced when analyzing experimental X-ray images, allowed us to obtain the dislocation viscosity coefficients, B. The B-values found in $LiNbO_3$ were 2–3 orders of magnitude lower than any value measured before in ductile materials. The results obtained for brittle ceramic crystals, such a $LiNbO_3$, prove that the technique developed significantly expands our abilities to investigate phonon interaction with dislocations.

At the same time, the models that were used rely on several approximations. The dynamic displacement maps were simulated for edge dislocation in isotropic material with the dislocation line parallel to the crystal surface. By taking X-ray images from different reflections, one can find the precise orientation and type of every dislocation in the image and after that perform more precise numerical simulations of the displacement maps using specific elastic constants of $LiNbO_3$. Using anisotropic models may lower the evaluated amplitudes of dislocation velocity by a factor of 2 or 3. In this case, the dislocation velocities are no longer "relativistic", but yet remain two orders of magnitude higher than any velocity value measured before in metals and alkali halides under acoustic wave excitation.

The extraction of the value of B by substituting the parameters obtained, ξ_0/λ and ϕ, into eq. (47) also relies on the approximated values of T or m^*. As pointed out by Seeger [46], the exact value of T can be numerically calculated if the dislocation orientation and character are known. Following Seeger's analysis [2,46], an increase of B by a factor of 2, due to some uncertainty in the T-values, may be considered. Finally, applying both corrections mentioned can raise the actual value of B by a factor of 5. This corrected value is still two orders of magnitude lower than any value measured until now in all materials investigated.

The experimental technique developed paves the route for further research in several directions. First, it is desirable to perform more accurate simulations of the dynamic displacement maps and to achieve more exact solutions for dislocation motion in order to have more accurate data on dislocation velocities and viscosity coefficients in brittle crystals. Secondly, the method developed [40] of applying stroboscopic X-ray imaging to

non-piezoelectric crystals opens the route for investigating dislocation interactions with phonons in a wide variety of semiconductor and optical crystals that are beyond the scope of other experimental methods. This can lead to the detection of new modes of dislocation vibration under acoustic wave excitation and can significantly expand the database of the viscosity coefficients, B, in different materials.

Stroboscopic X-ray diffraction imaging can also be applied for the very ambitious goal of investigating dislocation motions at relativistic velocities. According to eq. (47), the amplitude of dislocation vibration and, correspondingly, the dislocation velocity depends directly on the applied strain amplitude, ε_0^{eff}. Thus, a few times increase of the SAW amplitude (that is technically possible), in principle, may result in dislocation velocities very close to V_T.

The question of whether a dislocation can move faster than V_T is still open. Five decades ago Eshelby showed [47], basing on the theory of elasticity, that there exist solutions for the dislocation motion faster than V_T, that are accompanied by a strong emission of acoustic waves. For a long time, these solutions were considered to be unrealistic since the dislocation's energy infinitely increases at $V_d = V_T$. Thus, for decades no physical argument to overcome this infinitely high energy barrier was found. However, recent molecular dynamic simulations [48,49] have demonstrated that the dislocation velocity can overcome the barrier of V_T and can even be larger than the speed of longitudinal bulk waves. In these simulations, the dislocation velocities jumped over V_T within less than one ps time interval, i.e. when passing a distance of about one Burgers vector.

Dislocation velocities above V_T have never been observed experimentally. Apparently, nearly relativistic velocities were obtained by the application of a pulsed mechanical stress of about 0.01 μ in amplitude during about 1 μs [42]. Measurements of the dislocation positions before and after pulse application allowed us to calculate the average dislocation velocity but failed to provide any information about the dislocation behavior during this motion.

Applying the stroboscopic X-ray diffraction imaging to study the dislocation movements at relativistic velocities will provide important information not only on the limiting velocity itself but also on possible modifications of the dislocation strain fields at these velocities. Such experiments will open a new topic of research in dislocation mechanics.

References

[1] F.R.N. Nabarro, Theory of Crystal Dislocations (Oxford, University Press, 1967).
[2] A. Seeger, J. de Physique 42 (1981) C5-201.
[3] A.V. Granato and K. Lücke, in: Physical Acoustics, Vol. 4a, ed. W.P. Mason (Academic Press, London, 1966).
[4] G.A. Kneezel and A.V. Granato, Phys. Rev. B 25 (1982) 2581.
[5] G.A. Northrop, E.J. Cotts, A.C. Anderson and J.P. Wolfe, Phys. Rev. B 27 (1983) 6395.
[6] A.J. Slobodnik, Jr., in: Acoustic Surface Waves, ed. A.A. Oliner (Springer-Verlag, Berlin, 1978).
[7] A.A. Auld, Acoustic Fields and Waves in Solids (Krieger Publishing Company, Malabar, 1990).
[8] L.D. Landau and E.M. Lifshitz, Theory of Elasticity (Pergamon, Oxford, 1986).
[9] R.E. Peierls, Proc. Phys. Soc. London 52 (1940) 34.
[10] H. Alexander and P. Haasen, Solid State Physics 22 (1968) 28.
[11] A.I. Akhiezer, J. Phys. USSR 1 (1939) 277.

[12] W.P. Mason, J. Acoust. Soc. Am. 32 (1960) 458.
[13] W.P. Mason, Phys. Rev. 97 (1955) 557.
[14] V.A. Al'shitz and V.L. Indenbom, Sov. Phys.-Usp. 18 (1975) 1.
[15] V.A. Al'shitz, Sov. Phys.-Soild State 11 (1970) 1947.
[16] E. Nadgornyi, in: Progress in Materials Science, Vol. 31, eds J.W. Christian, P. Haasen and T.B. Massalski (Pergamon Press, New York, 1988).
[17] F. Fanti, J. Holder and A.V. Granato, J. Acoust. Soc. Am. 45 (1969) 1356.
[18] E.P. Roth and A.C. Anderson, Phys. Rev. B 20 (1979) 768.
[19] G.A. Northrop and J.P. Wolfe, Phys. Rev. B 22 (1980) 6196.
[20] D. Shilo and E. Zolotoyabko, Phys. Rev. Lett. 91 (2003) 115506.
[21] W.P. Mason, in: Physical Acoustics, Vol. 3b, ed. W.P. Mason (Academic Press, London, 1965).
[22] F.R.N. Nabarro and J.M. Ziman, Proc. Phys. Soc. London 78 (1961) 1512.
[23] J.M. Ziman, Electrons and Phonons (Oxford University Press, London, 1960) p. 228.
[24] A. Seeger and H. Bross, Z. Naturf. 15a (1960) 663.
[25] J.D. Eshelby, Proc. R. Soc. A197 (1949) 396.
[26] F.R.N. Nabarro, Proc. R. Soc. A209 (1951) 278.
[27] J.P. Hirth and J. Lothe, Theory of Dislocations (McGraw-Hill, 1968).
[28] A. Maurel, J.F. Mercier and F. Lund, Phys. Rev. B 70 (2004) 024303.
[29] H. Donth, Z. Phys. 149 (1957) 111.
[30] Y. Sugawara, O.B. Wright, O. Matsuda, M. Takigahira, Y. Tanaka, S. Tamura and V.E. Gusev, Phys. Rev. Lett. 88 (2002) 185504.
[31] J. Wolfe, Physics Today, 48 (1995) 34.
[32] D.V. Roschchupkin, M. Brunel and R. Tucoulou, J. Phys. IV 5 (1994) C5.
[33] E. Zolotoyabko, D. Shilo, W. Sauer, E. Pernot and J. Baruchel, Rev. Sci. Instrum. 70 (1999) 3341.
[34] R.W. Whatmore, P.A. Goddard, B.K. Tanner and G.F. Clark, Nature (London) 299 (1982) 44.
[35] H. Cerva and W. Graeff, Phys. Status Solidi A 82 (1984) 35.
[36] P.A. Goddard, G.F. Clark, B.K. Tanner and R.W. Whatmore, Nucl. Instrum. Methods 208 (1983) 705.
[37] E. Zolotoyabko, D. Shilo, W. Sauer, E. Pernot and J. Baruchel, Appl. Phys. Lett. 73 (1998) 2278.
[38] D. Shilo and E. Zolotoyabko, J. Phys. D 36 (2003) A122.
[39] E. Zolotoyabko, D. Shilo and E. Lakin, Mater. Sci. Eng. A309/310 (2001) 23.
[40] D. Shilo, E. Lakin, E. Zolotoyabko, J. Härtwig and J. Baruchel, Appl. Phys. Lett. 82 (2003) 1374.
[41] H. Matthews, Surface Wave Filters (John Wiley and Sons, New York, 1977).
[42] E. Gutmanas, private communication.
[43] E. Fries and A. Peter, Revue de Physique-Appliquēe 22 (1987) 1353.
[44] H.J. Levinstein and C.D. Capio, J. Appl. Phys. 38 (1967) 2761.
[45] D.V. Novikov, T. Gog, M. Griebenow, G. Materlik, I. Baumann and W. Sohler, Nucl. Instr. Meth. Phys. Res. B 97 (1995) 342.
[46] A. Seeger, private communication.
[47] J.D. Eshelby, Proc. Phys. Soc. London B69 (1956) 1013.
[48] P. Gumbsch and H. Gao, Science 283 (1999) 965.
[49] Q. Li and S. Shi, Appl. Phys. Lett. 80 (2002) 3069.